
SHORTEST-PATH FLOW MATCHING WITH MIXTURE-CONDITIONED BASES FOR OOD GENERALIZATION TO UNSEEN CONDITIONS

Andrea Rubbi^{‡,1,4} Amir Akbarnejad^{‡,1,5} Mohammad Vali Sanian^{‡,1,2,6} Aryan Yazdan Parast^{‡,3}
 Hesam Asadollahzadeh¹ Arian Amani¹ Naveed Akhtar³ Sarah Cooper¹
 Andrew Bassett¹ Pietro Liò⁴ Lassi Paavolainen² Sattar Vakili^{1,7}
 Mo Lotfollahi^{1,5,8}

¹Wellcome Sanger Institute, Cambridge, United Kingdom

²Institute for Molecular Medicine Finland (FIMM), University of Helsinki, Helsinki, Finland

³School of Computing and Information Systems, The University of Melbourne, Melbourne, Australia

⁴Department of Computer Science and Technology, University of Cambridge, Cambridge, United Kingdom

⁵Cambridge Centre for AI in Medicine, University of Cambridge, Cambridge, United Kingdom

⁶Department of Computer Science, University of Helsinki, Helsinki, Finland

⁷MediaTek Research, Cambridge, United Kingdom

⁸Cambridge Stem Cell Institute, University of Cambridge, Cambridge, United Kingdom

ABSTRACT

Robust generalization under distribution shift remains a key challenge for conditional generative modeling: conditional flow-based methods often fit the training conditions well but fail to extrapolate to unseen ones. We introduce **SP-FM**, a shortest-path flow-matching framework that improves out-of-distribution (OOD) generalization by conditioning both the base distribution and the flow field on the condition. Specifically, SP-FM learns a condition-dependent base distribution parameterized as a flexible, learnable mixture, together with a condition-dependent vector field trained via shortest-path flow matching. Conditioning the base allows the model to adapt its starting distribution across conditions, enabling smooth interpolation and more reliable extrapolation beyond the observed training range. We provide theoretical insights into the resulting conditional transport and show how mixture-conditioned bases enhance robustness under shift. Empirically, SP-FM is effective across heterogeneous domains, including predicting responses to unseen perturbations in single-cell transcriptomics and modeling treatment effects in high-content microscopy-based drug screening. Overall, SP-FM provides a simple yet effective plug-in strategy for improving conditional generative modeling and OOD generalization across diverse domains.

1 Introduction

Conditional generative models have achieved remarkable success across domains ranging from image synthesis to molecular design [Rombach et al., 2022, Ho and Salimans, 2021]. A common paradigm underlying many state-of-the-art approaches, including diffusion models and flow matching, is to learn a transport map from a simple base distribution to a complex target distribution, conditioned on some input descriptor [Lipman et al., 2022, Tong et al., 2023, Benamou and Brenier, 2000]. However, a critical limitation emerges when these models encounter conditions not seen during training: their performance degrades substantially, limiting their utility in real-world applications where exhaustive enumeration of all possible conditions is infeasible.

Out-of-distribution (OOD) generalization is particularly challenging in scientific applications because models are routinely asked to generate responses for *conditions that were never observed during training*. Here, we use *condition* to mean the *intervention or experimental setting* that indexes a data-generating distribution—for example a drug identity, a genetic perturbation, or a specific rotation of a letter—rather than a shift in the input instances of a predictor. Conditional

[‡]These authors contributed equally to this work.

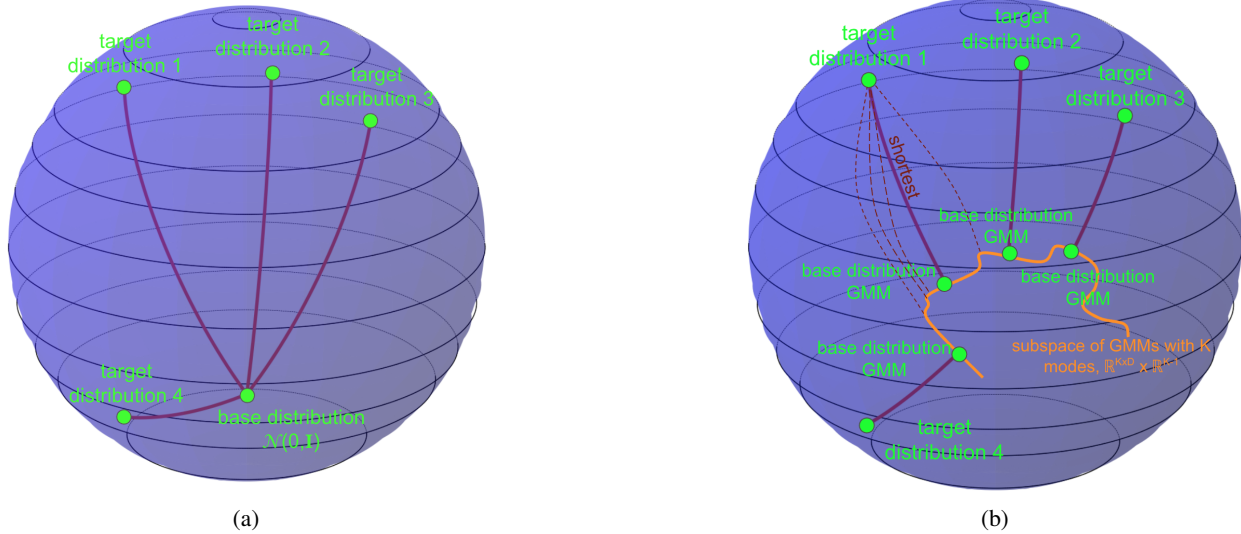


Figure 1: **Standard conditional flow matching versus SP-FM.** (a) Conventional approaches fix the base distribution to a standard Gaussian and condition only the velocity field on the descriptor y , effectively learning independent flows for each condition. (b) SP-FM conditions both the base distribution (as a Gaussian mixture) and the velocity field on the descriptor. For each target distribution, the base distribution is selected such that the length of the geodesic connecting the two is minimised. Similar conditions produce similar base distributions, requiring only small flow corrections and enabling smooth extrapolation to unseen conditions.

generative models are often brittle in this regime: they may interpolate within the training condition set but degrade sharply on truly held-out conditions, producing overly averaged samples or missing condition-specific effects.*

This issue appears across scientific domains. For example, in drug discovery one aims to predict cellular responses to novel compounds [Subramanian et al., 2017, Srivatsan et al., 2020]. Similarly, in genetic screening the goal is to predict phenotypic effects of unseen perturbations [Norman et al., 2019, Repleglo et al., 2022]. In such settings, the condition space (e.g., drugs, perturbations, compositions and their combinations) is combinatorially large, making exhaustive coverage impossible and forcing practical models to extrapolate beyond the training conditions. Consistent with this, recent benchmarks report that even sophisticated deep learning approaches often fail to outperform simple baselines when evaluated on truly held-out conditions [Ahlmann-Eltze et al., 2025], underscoring the difficulty of robust conditional generation under shift.

Why do current conditional generative models struggle with OOD conditions? We argue that the root cause lies in an overlooked architectural choice: *the base distribution is fixed*. Standard conditional flow matching and diffusion models use a fixed Gaussian $\mathcal{N}(0, I)$ as the source distribution, conditioning only the decoder (velocity field or score network) on the input descriptor [Lipman et al., 2022, Klein et al., 2025, Adduri et al., 2025]. This design implicitly treats each condition as an independent estimation problem: the model must learn a separate mapping from the same fixed base to each target distribution. When a novel condition arrives at test time, the model has no mechanism to leverage structural similarities with training conditions; it can only hope that the conditioned decoder generalizes due to, e.g., the decoder being smooth with respect to its input descriptor.

Recent work has begun to move beyond fixed base distributions, but along directions that differ from our objective. Chen et al. [2025] model the *velocity field* as a Gaussian mixture to enable efficient few-step sampling, without learning a condition-dependent base distribution. Atanackovic et al. [2024] propose Meta Flow Matching, which conditions the dynamics on an *observed initial population* encoded by a graph neural network, effectively assuming access to the starting distribution at test time and focusing on transferring dynamics across contexts. Other approaches construct application-specific priors to shorten transport paths and improve sampling efficiency [Bunne et al., 2023]. In contrast, SP-FM explicitly *learns* a condition-dependent base distribution jointly with the flow field, with the goal of improving OOD generalization to unseen conditions, and provides theoretical motivation for why conditioning the base can matter.

*In this paper, OOD generalization refers to generating from an unseen *condition* (intervention/setting) excluded from training, not to test-time covariate shift in predictor inputs. We assume the unseen condition is drawn from the same overall condition distribution.

We propose a different perspective: *the base distribution itself should be conditioned on the descriptor*. Our key insight is that when two conditions are similar, whether two rotation angles of images that differ by a small increment, two drugs with related chemical structures [Rogers and Hahn, 2010], or two genetic perturbations affecting the same pathway [Schubert et al., 2018], their corresponding target distributions are also likely to be similar. By learning a base distribution that reflects this similarity structure, we encode prior knowledge about condition relationships directly into the generative process. The flow then needs only to correct for the residual differences, rather than learning the entire mapping from scratch.

We introduce **SP-FM**, a conditional flow-matching framework that jointly learns a descriptor-conditioned Gaussian mixture base distribution and a descriptor-conditioned velocity field trained via shortest-path (optimal transport) flow matching. The key architectural change is simple: instead of sampling from a fixed Gaussian, SP-FM uses learned networks to predict condition-specific mixture parameters that define the base distribution. Samples from this adaptive base are then transported to the target via a learned velocity field. Because similar descriptors produce similar base distributions, the model can smoothly interpolate and extrapolate to unseen conditions, a capability that fixed-base approaches fundamentally lack.

We provide theoretical analysis supporting this design. Building on connections between flow matching and optimal transport [Peyré et al., 2019, Benamou and Brenier, 2000], we analyze the degrees of freedom in the transport problem as a function of the number of mixture components. We show that when the base is a single Gaussian, the dual optimal transport problem becomes ill-defined, providing a formal explanation for the poor generalization of vanilla conditional flow matching. With multiple mixture components, the problem becomes well-posed, and we derive bounds relating the base complexity, target complexity, and data dimension.

While conditional flow matching is often paired with domain-specific architectures and inductive biases (e.g., in single-cell [Klein et al., 2025] and morphology-based perturbation prediction [Navidi et al., 2024], [Zhang et al., 2025b]), our goal is a *general* improvement that can be plugged into existing pipelines. We therefore compare primarily to standard conditional flow-matching baselines under matched capacity and training budgets to avoid confounding gains from task-specific design choices. On synthetic rotated-letter benchmarks [Atanackovic et al., 2024], SP-FM improves generalization to unseen rotations. On image-based phenotypic assays [Cai et al., 2010, Sypetkowski et al., 2023, Bray et al., 2016], it reduces distributional distances when predicting morphologies under novel compound treatments. On single-cell transcriptomic datasets [Norman et al., 2019, Lotfollahi et al., 2023, Replogle et al., 2022], it accurately predicts gene-expression responses to unseen genetic and chemical perturbations.

1.1 Contributions

Our main contributions are:

- We identify the fixed base distribution as a key limiting factor for OOD generalization in conditional flow matching and propose MixFlow, which jointly learns a descriptor-conditioned Gaussian mixture base and a shortest-path velocity field.
- We provide theoretical analysis showing that single-Gaussian bases lead to ill-posed inference, while mixture bases with sufficient components yield well-defined problems with bounded estimation error.
- We demonstrate consistent improvements over conditional flow matching across eight datasets spanning synthetic, image-based, and transcriptomic domains, establishing SP-FM as a flexible framework for conditional generation with improved OOD generalization.

1.2 Related Work

Flow Matching and Continuous Normalizing Flows. Flow matching has emerged as a scalable framework for training continuous normalizing flows by regressing onto conditional velocity fields along interpolation paths between base and target distributions [Lipman et al., 2022]. Unlike score-based diffusion models that require simulating stochastic differential equations, flow matching enables simulation-free training and deterministic sampling via ordinary differential equations. Extensions have incorporated optimal transport couplings to straighten trajectories and improve sample efficiency [Tong et al., 2023, Benamou and Brenier, 2000], while others have explored Riemannian geometries and alternative path constructions [Peyré et al., 2019]. A key limitation shared by these approaches is the reliance on a fixed base distribution—typically a standard Gaussian—which we argue fundamentally limits generalization to unseen conditions.

Conditional Generative Models. Conditioning generative models on auxiliary information has enabled applications from class-conditional image synthesis [Ho and Salimans, 2021, Rombach et al., 2022] to text-to-image generation.

In scientific domains, conditional models have been applied to predict cellular responses to perturbations [Lotfollahi et al., 2023, Hetzel et al., 2022, Roohani et al., 2024], model molecular dynamics [Bunne et al., 2023], and generate cell morphologies [Palma et al., 2025, Navidi et al., 2024, Zhang et al., 2025b]. Recent flow-based approaches include CellFlow [Klein et al., 2025], which applies flow matching to single-cell phenotype modeling, and STATE [Adduri et al., 2025], a transformer-based architecture for context-aware perturbation prediction. These methods condition the velocity field or decoder on perturbation descriptors but maintain a fixed base distribution, treating each condition as an effectively independent estimation problem. Despite their success in different domains, generative models generalization remains a puzzling phenomenon Bertrand et al. [2025]. For example, a line of research shows that generative models may learn to merely generative training instances, failing to generate novel samples and risking privacy issues when trained on licenced or sensitive medical data Yoon et al. [2023], Bertrand et al. [2025], Bamberger et al. [2025]. Besides the memorisation viewpoint, one can see the lack of generalisation from the lens of score estimation Song and Ermon [2019], where the generative model is shown to learn an independent score estimator for each descriptor in the training set and its corresponding population, as well as for the combined population Ho and Salimans [2021]. In this case, the independent score estimators are not expected to generalise to unseen descriptors.

Gaussian Mixtures in Generative Models. Gaussian mixture models (GMMs) have a long history as flexible density estimators with universal approximation properties [Nguyen, 2019, Zheng and Tang, 2020]. Recent work has revisited GMMs in the context of modern generative models. Chen et al. [2025] propose GMFlow, which models the *velocity distribution* as a Gaussian mixture to capture multimodal flow directions, improving few-step sampling and reducing over-saturation artifacts. Ahamed et al. [2025] use GMMs in latent spaces for molecular generation. These approaches modify how the velocity or score is represented but do not condition the *base distribution* on input descriptors. In contrast, SP-FMlearns a descriptor-conditioned GMM as the source distribution, explicitly encoding condition similarity structure to improve OOD generalization.

Learned and Adaptive Prior Distributions. Several works have explored moving beyond fixed Gaussian priors. In the context of variational autoencoders, learned priors have been used to improve expressiveness [Bereket and Karaletsos, 2023]. For flow-based models, Bunne et al. [2023] learn transport maps via neural optimal transport for single-cell perturbation modeling, though with a focus on paired control-treatment settings rather than OOD generalization. Meta Flow Matching [Atanackovic et al., 2024] conditions on initial populations by embedding them via graph neural networks, enabling generalization across different starting distributions on the Wasserstein manifold. This approach is complementary to ours: while Meta Flow Matching learns to adapt to varying initial populations, SP-FMlearns to predict appropriate base distributions from condition descriptors, directly targeting the OOD generalization problem.

Out-of-Distribution Generalization. OOD generalization remains a central challenge in machine learning, with extensive work on domain adaptation, invariant learning, and distributionally robust optimization. In the context of perturbation biology, recent analyses have shown that deep learning models often fail to generalize beyond training perturbations, sometimes underperforming simple linear baselines [Ahlmann-Eltze et al., 2025]. This has motivated the development of methods that explicitly encode biological structure, such as pathway information [Roohani et al., 2024] or chemical similarity [Subramanian et al., 2017, Wang et al., 2016]. SP-FMtakes a complementary approach by encoding similarity structure directly into the generative model architecture through the learned base distribution, providing a general mechanism for OOD generalization that does not require domain-specific inductive biases.

2 Problem Setup

We study population-level generative modelling. Let $\{\rho_1, \dots, \rho_N\}$ denote N probability measures on \mathbb{R}^D , each corresponding to a distinct population. For each $n \in \{1, \dots, N\}$ we observe a dataset

$$\mathcal{X}_n = \{\mathbf{x}_{n,1}, \dots, \mathbf{x}_{n,s_n}\} \subset \mathbb{R}^D,$$

consisting of s_n samples drawn i.i.d. from ρ_n . Each population is associated with a descriptor $\mathbf{y}_n \in \mathcal{Y}$ that encodes metadata about the population (e.g., the rotation angle of a letter, perturbation applied to cells, a molecular embedding of a drug, or cell-type information).

Given training data $\{(\mathcal{X}_n, \mathbf{y}_n)\}_{n=1}^N$, the aim is to learn a conditional generative model that produces samples from ρ_n when provided with \mathbf{y}_n . At test time, the model is presented with an unseen descriptor \mathbf{y}_{test} and must generate samples approximating the corresponding, unknown distribution ρ_{test} . This setup captures, for example, predicting the distribution of gene expression states under new perturbations, conditioned on information about the perturbation, baseline cells, and biological experimental conditions.

2.1 Background on Conditional Flow Matching

Flow matching provides a scalable framework for learning conditional generative models that map a simple base distribution to a potentially-complex one.

Flow-based generative models. A flow model generates a target distribution ρ by transporting a simple base distribution μ (e.g. a standard Gaussian) along the trajectories of an ODE. Let $v : \mathbb{R}^D \times [0, 1] \rightarrow \mathbb{R}^D$ be a time-dependent velocity field and consider

$$\frac{d}{dt} \mathbf{x}_t = v(\mathbf{x}_t, t), \quad \mathbf{x}_0 \sim \mu. \quad (1)$$

The measure on \mathbf{x}_t is denoted by ρ_t , which evolves according to the continuity equation:

$$\partial_t \rho_t = -\nabla \cdot (\rho_t v(\cdot, t)), \quad \rho_0 = \mu. \quad (2)$$

With an appropriate choice of v , the terminal distribution ρ_1 coincides with the target ρ .

Conditional flows. To capture population variability, we parameterize a conditional velocity field

$$v_\theta : \mathbb{R}^D \times [0, 1] \times \mathcal{Y} \rightarrow \mathbb{R}^D,$$

and define the dynamics

$$\frac{d}{dt} \mathbf{x}_t = v_\theta(\mathbf{x}_t, t; \mathbf{y}), \quad \mathbf{x}_0 \sim q. \quad (3)$$

For a descriptor \mathbf{y}_n , the terminal distribution of this flow, denoted $\rho_{1,\theta}(\cdot | \mathbf{y}_n)$, should approximate ρ_n . At test time, for a novel descriptor \mathbf{y}_{test} , the model produces $\rho_{1,\theta}(\cdot | \mathbf{y}_{\text{test}})$ as an approximation to ρ_{test} .

Flow matching objective. Training v_θ is performed by regression to a teacher velocity field that imposes the boundary conditions (*i.e.* the conditions $\rho_0 = \mu$ and $\rho_1 = \rho$) along with potentially other conditions to, *e.g.*, regularise the flow model. The teacher flow is constructed by integrating over interpolant paths between the base μ and the empirical populations ρ_n , while the training is shown to be feasible by individual interpolant paths Lipman et al. [2022]. Specifically, let $(\mathbf{x}_0, \mathbf{x}_1) \sim \mu \otimes \rho_n$, *i.e.* $\mathbf{x}_0 \sim \mu$ and $\mathbf{x}_1 \sim \rho_n$ independently, and consider the linear interpolant

$$\mathbf{x}_t = (1-t)\mathbf{x}_0 + t\mathbf{x}_1, \quad t \in [0, 1].$$

The individual conditional teacher interpolant path is defined as

$$u(\mathbf{x}_t, t | \mathbf{x}_0, \mathbf{x}_1) = \mathbf{x}_1 - \mathbf{x}_0. \quad (4)$$

More advanced constructions use Wasserstein geodesic interpolants [Benamou and Brenier, 2000, Peyré et al., 2019, Tong et al., 2023], which provide velocity fields aligned with optimal transport.

The conditional flow matching loss is then

$$\mathcal{L}(\theta) = \frac{1}{N} \sum_{n=1}^N \mathbb{E}_{t \sim \text{Unif}[0,1]} \mathbb{E}_{(\mathbf{x}_0, \mathbf{x}_1) \sim \mu \otimes \rho_n} \|v_\theta((1-t)\mathbf{x}_0 + t\mathbf{x}_1, t; \mathbf{y}_n) - (\mathbf{x}_1 - \mathbf{x}_0)\|^2. \quad (5)$$

Minimizing equation 5 learns a parametric family of velocity fields that transports the base distribution μ to each ρ_n , while sharing parameters across populations through conditioning on \mathbf{y}_n .

3 Mixture-Conditioned Flow Matching

Standard conditional flow matching fixes the base distribution to $\mathcal{N}(\mathbf{0}_D, \sigma^2 \mathbf{I}_{D \times D})$ and conditions only the decoder, effectively yielding independent estimators for each population and limiting generalization (See, Fig. 1a). SP-FM instead conditions both the base distribution and the flow module on perturbations and covariates (Fig. 1b).

Let I denote the number of mixture components. Plausible base distributions are Gaussian mixtures $\mu_{\text{GMM}(\Theta, \mathbf{p})}$ with $\Theta \in \mathbb{R}^{I \times D}$ specifying mode locations, $\mathbf{p} \in \mathbb{S}^{I-1}$ specifying mixture weights, and fixed component variance σ^2 . The family of such mixtures forms the restricted subspace illustrated in Fig. 1b in orange.

Given populations $\{\rho_1, \dots, \rho_N\}$ with descriptors $\{\mathbf{y}_1, \dots, \mathbf{y}_N\}$, each ρ_n is projected to its closest element $\mu_{\text{GMM}(\Theta^{(n)}, \mathbf{p}^{(n)})}$ in this subspace. The optimal transport to ρ_n from its projection defines a velocity field $v(\cdot, t; \mathbf{y}_n)$. These velocity fields form geodesics on the 2-Wasserstein manifold of probability measures, which are shown by the red curves in Fig. 1b. Predictors $h_\Theta : \mathcal{Y} \rightarrow \mathbb{R}^{I \times D}$ and $h_\mathbf{p} : \mathcal{Y} \rightarrow \mathbb{S}^{I-1}$ are trained so that $h_\Theta(\mathbf{y}_n) \approx \Theta^{(n)}$ and $h_\mathbf{p}(\mathbf{y}_n) \approx \mathbf{p}^{(n)}$. At test time, the predicted base $\mu_{\text{GMM}(h_\Theta(\mathbf{y}_{\text{test}}), h_\mathbf{p}(\mathbf{y}_{\text{test}}))}$ is evolved by $v(\cdot, t; \mathbf{y}_{\text{test}})$ to approximate ρ_{test} .

3.1 Training objectives

SP-FM is trained with two complementary losses.

Objective 1. Align the learned velocity field $v_\theta(., t; \mathbf{y}_n)$ with the OT path between ρ_n and its projected base:

$$\mathcal{L}_{\text{OT}} = \mathbb{E} \left[\sum_{s=1}^S \|v\left(t, (1-t)\mathbf{x}_s^{(0)} + t\mathbf{x}_{\tau(s)}, \mathbf{y}_n\right) - (\mathbf{x}_{\tau(s)} - \mathbf{x}_s^{(0)})\|^2 \right], \quad (6)$$

where $\{\mathbf{x}_s\} \sim \rho_n$, $\{\mathbf{x}_s^{(0)}\} \sim \mu_{\text{GMM}(h_\Theta(\mathbf{y}_n), h_p(\mathbf{y}_n))}$, $t \sim \text{Unif}(0, 1)$, and τ denotes mini-batch OT pairing [Tong et al., 2023].

Objective 2. Encourage each projection $\mu_{\text{GMM}(h_\Theta(\mathbf{y}_n), h_p(\mathbf{y}_n))}$ to remain close to ρ_n by minimizing geodesic length:

$$\mathcal{L}_{\text{geo}} = \mathbb{E} \left[\sum_{s=1}^S \|\mathbf{x}_{\tau(s)} - \mathbf{x}_s^{(0)}\|^2 \right], \quad (7)$$

with the Gumbel–softmax trick ensuring differentiability with respect to mixture weights and mode locations.

The training procedure is elaborated in Alg. 1, where the training alternates between updating the flow model in line 19 and the base distributions in line 22. In Alg. 1 the training planner P divides the training into three parts: (i) warm-up period, where only the flow model is updated, (ii) alternating period, during which after a certain number of updates to the flow model, a single update is made to the base distributions. (iii) cool-down period, where the base distributions are kept fixed and only the flow model is trained. Notably, during the warm-up and alternating periods the dropout layers of H_Θ and H_p are enabled, while in the cool-down period they are disabled.

3.2 Inference

At test time, given a novel descriptor \mathbf{y}_{test} , SP-FM predicts the base distribution $\mu_{\text{GMM}(h_\Theta(\mathbf{y}_{\text{test}}), h_p(\mathbf{y}_{\text{test}}))}$ and evolves it with $v(., t; \mathbf{y}_{\text{test}})$, $t \in [0, 1]$ to generate samples approximating ρ_{test} .

4 Generalization Analysis

The Wasserstein manifold of probability measures is infinite-dimensional, hindering the adoption of theoretical generalization guarantees for finite-dimensional spaces. To circumvent this, we assume that the target distribution ρ is itself a Gaussian mixture model (GMM) with J components,

$$\rho = \rho_{\text{GMM}(\mathbf{\Gamma}, \mathbf{q})},$$

where $\mathbf{\Gamma} \in \mathbb{R}^{J \times D}$ are fixed mode locations, $\mathbf{q} \in \mathbb{S}^{J-1}$ are mixture weights, and all components share a fixed variance. This setting still captures highly general distributions: as $J \rightarrow \infty$ and $\mathbf{\Gamma}$ forms a sufficiently fine grid covering \mathbb{R}^D , the family $\text{GMM}(\mathbf{\Gamma}, \mathbf{q})$ is dense in the space of probability measures under the Wasserstein metric [Nguyen, 2019, Zheng and Tang, 2020]. Thus, assuming ρ is GMM-induced is a broad and flexible modelling assumption. In this formulation, prediction reduces to estimating the mixture weights $\mathbf{q} \in \mathbb{S}^{J-1}$ from the population descriptor \mathbf{y} .

A naive solution is to directly learn a predictor mapping $\mathbf{y} \mapsto \mathbf{q}$. However, this approach suffers from poor generalization as J grows, since the dimensionality of \mathbf{q} directly affects the generalization. MixFlow instead takes a structured approach: rather than predicting \mathbf{q} directly, it (i) projects the target distribution onto the subspace of GMMs with I components (possibly, $I \ll J$), and (ii) learns the velocity field that transports this projection to the target distribution.

Besides the aforementioned assumptions, in the theoretical analysis we assume that this 2-step algorithm uses mixture Wasserstein distance [Delon and Desolneux, 2020, Bing et al., 2022] and the flow model induced by it, as opposed to the commonly used 2-Wasserstein distance. In the latter case, the pushforward function of the flow model can map its input points to any arbitrary point in \mathbb{R}^D . While in the former case, a discrete optimal transport problem is solved between the source and target GMMs to determine, intuitively, how the modes of the source GMM should be moved or split to create the target GMM, and that fully determines the flow. In this sense, the latter metric and flow model are a generalisation of the former. Nonetheless, this analysis highlights the importance of conditioning the base distribution on population descriptor \mathbf{y} , which we experimentally validate in in Sec. 6.

In this section we only summarize the key theoretical findings. Details are provided in Appendix A.

Statement 1 (Summary of theoretical findings). *Recall that $I, J, D \in \mathbb{N}$ are respectively the number of modes in the base and target GMM distributions, and the data dimension.*

Algorithm 1 Training SP-FM with mixture-conditioned flow matching

Require: Datasets $\{(\mathbf{X}_n, \mathbf{y}_n)\}_{n=1}^N$, number of base GMM modes I , fixed GMM variances σ^2 , training planner P .

- 1: Initialize parameters: $params(v(\cdot, \cdot, \cdot))$ (velocity field), $params(h_{\Theta}(\cdot))$ (mode position predictor), and $params(h_p(\cdot))$ (mode probability predictor), learning rate ℓ .
- 2: $cnt_epoch \leftarrow 0$
- 3: $cnt_iteration \leftarrow 0$
- 4: **for** each training epoch **do**
- 5: **while** the epoch hasn't finished **do**
- 6: $mode_train, flag_settoeval_H \leftarrow P.next(cnt_epoch, cnt_iteration)$
- 7: Sample a population $(\mathbf{X}_n, \mathbf{y}_n)$
- 8: $\{\mathbf{x}_s\}_{s=1}^S \leftarrow S$ samples from the selected population
- 9: $\{\mathbf{x}_s^{(0)}\}_{s=1}^S \leftarrow S$ Samples from $\mu_{GMM(h_{\Theta}(\mathbf{y}_n), h_p(\mathbf{y}_n))}$
- 10: $\tau \leftarrow$ mini-batch discrete OT pairing between $\{\mathbf{x}_s\}_{s=1}^S$ and $\{\mathbf{x}_s^{(0)}\}_{s=1}^S$
- 11: **if** $flag_settoeval_H$ **then**
- 12: $H_{\Theta}.eval(); H_p.eval()$ ▷ i.e. disable dropout
- 13: **else**
- 14: $H_{\Theta}.train(); H_p.train()$ ▷ i.e. enable dropout
- 15: **end if**
- 16: **if** $mode_train$ equals 'velocity field' **then**
- 17: $t \leftarrow unif(0, 1)$
- 18: $\mathcal{L}_{OT} \leftarrow$ compute according to Eq. 6
- 19: $params(v(\cdot, \cdot, \cdot)) \leftarrow params(v(\cdot, \cdot, \cdot)) - \ell \cdot \nabla \mathcal{L}_{OT}$
- 20: **else if** $mode_train$ equals 'base distribution' **then**
- 21: $\mathcal{L}_{geo} \leftarrow$ compute according to Eq. 7
- 22: $params(H_{\Theta}, H_p) \leftarrow params(H_{\Theta}, H_p) - \ell \cdot \nabla \mathcal{L}_{geo}$
- 23: **else**
- 24: "print(ERROR: unknown value for mode_train)"
- 25: **end if**
- 26: $cnt_iteration \leftarrow cnt_iteration + 1$
- 27: **end while**
- 28: $cnt_epoch \leftarrow cnt_epoch + 1$
- 29: **end for**

§1 In the testing phase, the velocity field $\mathbf{V} \in \mathbb{R}^{I \times J}$ is identified up to $J - ID$ degrees of freedom. In particular, if $I \geq \lceil J/D \rceil$, then \mathbf{V} is uniquely identified.

§2 If $I = 1$, the problem reduces to predicting the J mixture weights \mathbf{q} directly from \mathbf{y} , corresponding to the common baseline of fixing the base distribution to $\mathcal{N}(\mathbf{0}_D, \mathbf{I}_{D \times D})$ and explaining its poor generalization.

Essentially, Statement 1 suggests that increasing the number I of modes of the base distribution by one, reduces degrees of freedom of the flow model by the data dimension D , thereby facilitating the prediction and identification of the flow model in the testing phase.

5 Experiments

We evaluate SP-FM against Vanilla Conditional Flow Matching (Vanilla CFM) on a set of synthetic and experimental datasets. Our goal is to assess SP-FM's generalizability and its robustness across multiple conditions, datasets, and hyperparameters. We seek empirical evidence of the need for the Gaussian Mixture Model (GMM) to describe the base distribution and its impact on the distributional distance between the inferred final distributions and the empirical ones.

5.1 SP-FM on Synthetic Data

Following Meta Flow Matching [Atanackovic et al., 2024], we create a synthetic benchmark of populations $\{(\rho_i, \mathbf{y}_i)\}$ where each condition i corresponds to a target population $\rho_i = p_1(x_1 \mid i)$ supported on a rendered letter silhouette. For every alphabet character we generate 20 rotations; each (letter, rotation) pair defines one condition (*i.e.* one descriptor \mathbf{y}_i) and its corresponding population. The descriptor \mathbf{y}_i is the concatenation of a one-hot letter code and a normalized rotation value. The target population ρ_i is formed by sampling uniformly from the foreground pixels of the silhouette.

To ensure that each condition corresponds to a full population rather than a single sample, we render multiple copies of the same silhouette using different fixed RGB colours. These colour variations are used only to generate several samples per condition and are not included in the descriptor \mathbf{y}_i .

For SP-FM, we construct a mixture-conditioned base for each population. We set the number of base modes I equal to the number of conditions and assign one Gaussian component per condition. In our synthetic setup, we do not use $h_{\Theta}(\mathbf{y}_i)$ to predict the component means; instead, the GMM mode locations are implemented as free learnable parameters, each initialized from a single rendered sample of its corresponding condition. The mixture weights are still predicted by the MLP $h_p(\mathbf{y}_i)$. The velocity field $v(\cdot, t; \mathbf{y}_i)$ is then trained using the flow-matching objectives in Eqs. 6–7 to transport the resulting $\mu_{\text{GMM}(\Theta^{(i)}, h_p(\mathbf{y}_i))}$ toward ρ_i . As a baseline, conditional flow matching (CFM) fixes the base to $\mathcal{N}(\mathbf{0}_D, \mathbf{I}_{D \times D})$ and samples $x_0 \sim \mathcal{N}(\mathbf{0}, \mathbf{I})$ at generation time.

We train SP-FM and all baselines on a synthetic dataset of 6 letters with $R = 20$ rotations per letter, and study rotation interpolation generalization. Specifically, we generate R rotation angles uniformly spaced in $[0, 2\pi]$ and split them by index: the training set contains the 10 even-indexed rotations, while the held-out set contains the 10 odd-indexed rotations. We form the validation set by selecting a single `val_letter` and evaluating that letter only on the held-out (odd-indexed) rotations; all letters (including `val_letter`) are present in training but only at the even-indexed rotations. In the main paper we report results with `val_letter` = S, and evaluate generalization on two unseen test letters, W and Y, each measured on their held-out (odd-indexed) rotations. To ensure conclusions are not tied to a particular character geometry, we repeat the same protocol with different choices of validation letter; results for `val_letter` = H are reported in the appendix. Results are reported in Table 1, with qualitative samples in Figure 2.

We compare SP-FM against three baselines: (i) **CFM**, which uses a fixed isotropic Gaussian base; (ii) a **conditional GMM** baseline that learns a mixture model by expectation-maximization (EM) algorithm with condition-dependent mixture weights $\pi(\cdot | \mathbf{y})$ (implemented as a learned lookup table over conditions) and shared component parameters, but does not learn a transport map; and (iii) **SP-FM (K=1)**, an ablation where SP-FM is restricted to a single mixture component, reducing the base distribution to a unimodal Gaussian (learnable mean) and testing whether improved performance can be explained by a single adaptive mode alone. These baselines isolate the contributions of the two key ingredients in SP-FM: learning a condition-adaptive multi-modal base distribution and learning a conditional transport field.

For each setting, we select the best checkpoint based on the validation W2 distance and report all metrics at this checkpoint. Table 1 shows that SP-FM consistently outperforms all baselines across validation on S and testing on W and Y, demonstrating the effectiveness of mixture-conditioned flow matching for rotation-interpolation generalization. Importantly, the relative behavior of the baselines also highlights the contribution of each component: SP-FM (K=1) underperforms, indicating that a unimodal (single-mode) base is insufficient even when it is learnable, while the conditional GMM (EM) baseline underperforms SP-FM, indicating that adapting the base distribution alone (via $\pi(\cdot | \mathbf{y})$) is not enough without learning the subsequent transport field. Consistent with the training objective that explicitly encourages the predicted base to stay close to the target (Eq. 7), the Source vs. Target metrics are improved under SP-FM, providing direct empirical evidence that the learned source distribution is already similar to the target before transport. This behavior is also visible qualitatively in Figure 2: SP-FM starts from a source distribution that resembles the target shape and produces smoother, more faithful trajectories, whereas CFM exhibits larger mismatch at $t = 0$ and more pronounced distortions along the path. Implementation details and hyperparameters for SP-FM and all baselines are provided in Appendix ??.

5.2 Using SP-FM to predict single-cell responses for unseen interventions

Single-cell perturbation screenings are an invaluable tool for new treatment discovery; they consist in testing the effects of genetic or chemical perturbations on cells in vitro. Each cell is exposed to a specific condition, and its gene expression is measured to assess whether the perturbation is associated with a given phenotypic change. We evaluate whether SP-FM can predict cellular responses to perturbations never observed before.

Models are trained on a subset of conditions and tested on held-out ones, defining an *out-of-distribution (OOD) generalisation* problem. Table 2 provides an overview of the datasets used in our experiments. Notably, Combo-Sciplex [Lotfollahi et al., 2023] and Norman [Norman et al., 2019] datasets also contain combinations of two perturbations. For each dataset, we generate four random splits, holding out 70% of the perturbations from the training set. Given the larger number of cells available in the iAstrocytes and Replogle-Nadig [Replogle et al., 2022] datasets, we guarantee high reliability of our results by filtering for conditions with at least 300 and 500 cells, respectively. The iAstrocytes data has been produced in-house in Sanger Institute, and it is not currently publicly available.

We report Wasserstein-1, Wasserstein-2, MMD, and Energy distances (ED). These metrics assess whether predicted distributions accurately capture the global geometry of observed cell states, beyond low-order statistics. On all tested

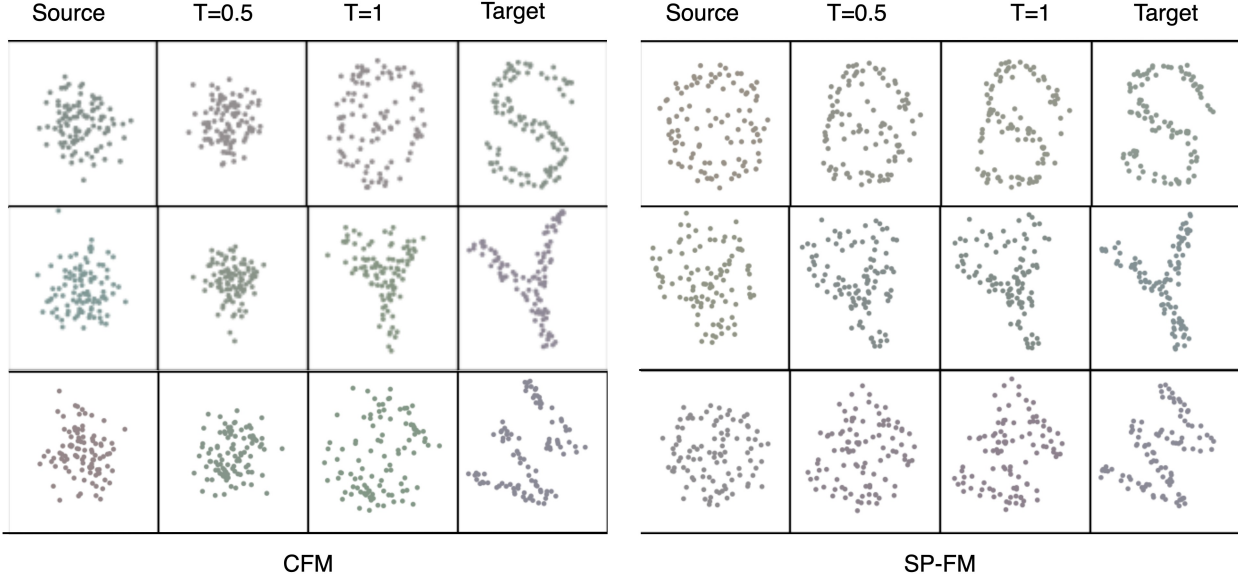


Figure 2: Qualitative comparison of Conditional Flow Matching (CFM) and SP-FM on the synthetic letter–rotation benchmark. Each block shows samples at different integration times ($t = 0$, $t = 0.5$, $t = 1$) and the corresponding target distribution. SP-FM produces smoother trajectories and more faithful reconstructions on unseen rotations, while CFM exhibits drift and shape distortion.

Table 1: Synthetic letter–rotation benchmark. Models are trained on even-indexed rotations and validated on S using held-out odd-indexed rotations; results are reported for S and unseen rotations on test letters W and Y. We report both Generated vs. Target and *Source* vs. *Target* distances. The conditional GMM baseline is trained via EM (no validation checkpoint), and since it has no flow model its *Source* vs. *Target* equals Generated vs. *Target*, so only the latter is reported.

Dataset	Model	Generated vs. Target			Source vs. Target		
		MMD \downarrow	W1 \downarrow	W2 \downarrow	MMD \downarrow	W1 \downarrow	W2 \downarrow
Letter S (Val)	CFM	0.01627 \pm 0.00069	0.5874 \pm 0.0199	0.7071 \pm 0.0266	0.08249 \pm 0.00138	1.0671 \pm 0.0076	1.1898 \pm 0.0069
	SP-FM	0.00986 \pm 0.00014	0.4740 \pm 0.0028	0.5744 \pm 0.0006	0.01986 \pm 0.00008	0.6464 \pm 0.0014	0.7388 \pm 0.0005
	SP-FM (I=1)	–	–	–	–	–	–
Letter W (Test)	CFM	0.01809 \pm 0.00081	0.6180 \pm 0.0141	0.7283 \pm 0.0152	0.06088 \pm 0.00049	0.8972 \pm 0.0062	1.0151 \pm 0.0071
	SP-FM (I=60)	0.01279 \pm 0.00131	0.5323 \pm 0.0203	0.6310 \pm 0.0223	0.01825 \pm 0.00062	0.6101 \pm 0.0067	0.7126 \pm 0.0061
	GMM (I=600)	0.08931 \pm 0.00387	1.1311 \pm 0.0299	1.3202 \pm 0.0375	–	–	–
	SP-FM (I=1)	–	–	–	–	–	–
Letter Y (Test)	CFM	0.02333 \pm 0.00197	0.6278 \pm 0.0160	0.7415 \pm 0.0176	0.06020 \pm 0.00128	1.0614 \pm 0.0048	1.2410 \pm 0.0054
	SP-FM (I=60)	0.01799 \pm 0.00015	0.5433 \pm 0.0044	0.6403 \pm 0.0064	0.04079 \pm 0.00225	0.9336 \pm 0.0297	1.0861 \pm 0.0312
	GMM (I=600)	0.07423 \pm 0.00528	0.8986 \pm 0.0317	1.0508 \pm 0.0417	–	–	–
	SP-FM (I=1)	–	–	–	–	–	–

single-cell perturbation datasets, SP-FM achieves substantially stronger distributional alignment than Vanilla CFM (Table 3), showing how SP-FM better generalises when generating previously unseen conditions, across both genetic and chemical perturbation modalities.

5.3 SP-FM predicts unseen intervention responses in image-based assays

To extend beyond transcriptomic data, we evaluate SP-FM in an image-based drug discovery setting. High-content imaging provides rich phenotypic readouts, but exhaustive compound testing is infeasible. We therefore train on a subset of compounds and predict cell morphologies for unseen compounds using only their chemical representations at test time.

We benchmark on BBB021 Caie et al. [2010] and RxRx1 Sypetkowski et al. [2023], comparing SP-FM against a conditional flow matching baseline (CFM). Table 4 shows that SP-FM achieves consistently lower distance metrics (MMD, W1, W2, ED), indicating more faithful recovery of unseen phenotypic responses. We split BBB021 following

Table 2: Single-cell perturbation datasets used to evaluate SP-FM.

Dataset	Cells	Perturbations	Cell type
Norman [Norman et al., 2019]	~90k	277 CRISPR*	K562
Combo-Sciplex [Lotfollahi et al., 2023]	~70k	32 compounds*	A549
iAstrocytes	~150k	148 CRISPR	iAstrocytes
Replogle–Nadig [Replogle et al., 2022]	~250k	67 CRISPRi	Jurkat
BBBC021 [Cai et al., 2010]	97,504 images	35 compounds	MCF7
RxRx1 [Sypetkowski et al., 2023]	170,193 images	1066 siRNA	U2OS

* single or paired perturbations.

Table 3: Cell-type perturbation benchmarks comparing SP-FM and CFM. Mean \pm std over four runs. Lower is better.

Dataset	Model	MMD \downarrow	W1 \downarrow	W2 \downarrow	ED \downarrow
Norman	CFM	0.199 ± 0.009	30.449 ± 0.241	467.8 ± 8.1	16.2 ± 0.3
	SP-FM	0.192 ± 0.004	30.084 ± 0.284	456.3 ± 9.1	15.9 ± 0.3
Combo-SciPlex	CFM	0.141 ± 0.005	26.007 ± 0.464	344.8 ± 12.6	9.0 ± 0.3
	SP-FM	0.129 ± 0.006	25.640 ± 0.180	335.3 ± 4.8	8.5 ± 0.2
iAstrocytes	CFM	0.163 ± 0.003	27.121 ± 0.110	369.7 ± 3.0	13.2 ± 0.1
	SP-FM	0.135 ± 0.004	27.061 ± 0.233	367.6 ± 6.5	12.6 ± 0.1
Replogle (Jurkat)	CFM	0.116 ± 0.006	52.919 ± 0.200	1408.3 ± 10.6	28.0 ± 0.3
	SP-FM	0.095 ± 0.003	52.868 ± 0.215	1404.9 ± 11.5	27.3 ± 0.4

prior work [Palma et al., 2025]: training uses 25 compounds and testing 9. For RxRx1, we train on 853 siRNAs and test on 213.

A key design choice is to generate instances in *feature space* rather than pixel space. Images are encoded with DINOv2 [Oquab et al., 2024] into 768-D embeddings, which aligns with semantically meaningful morphology-level distances [Oquab et al., 2024, Zhang et al., 2018]. This strategy improves efficiency, imposes a semantic inductive bias, and enables geometry-aware evaluation. For fairness, CFM outputs are also scored in the same DINOv2 feature space. Results are provided in Table 4. These substantial gains indicate that SP-FM more faithfully recovers unseen compound phenotypes, highlighting its potential to reduce experimental burden through reliable *in silico* prediction.

6 Ablations

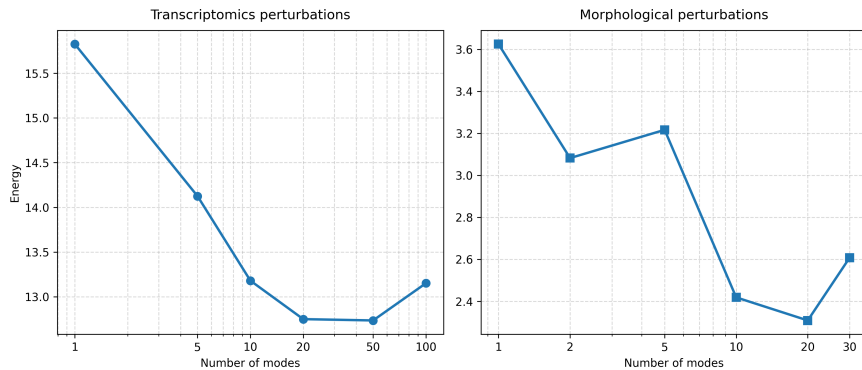
We conduct ablation studies to understand the key design choices in SP-FM. All experiments are performed on both transcriptomic (iAstrocytes) and morphological (BBBC021) datasets to ensure findings generalize across modalities.

Number of mixture components. A central design choice in SP-FM is the number of modes I in the Gaussian mixture base distribution. We vary I (the number of modes) and measure the energy distance between generated and ground-truth distributions on held-out perturbations. As shown in Figure 3a, increasing the number of modes consistently improves performance up to a point: energy distance decreases as I grows, reflecting the increased expressiveness of the base distribution. However, beyond a dataset-dependent threshold, performance plateaus or slightly degrades. We attribute this to optimization difficulty: with too many modes, the model must learn to allocate probability mass across components that may not be necessary, increasing the effective number of parameters without proportional benefit. Notably, the optimal I differs between datasets (transcriptomic data benefits from more modes than morphological data) suggesting that the appropriate complexity of the base distribution should reflect the heterogeneity of the target populations. These findings align with our theoretical analysis in Section 4: increasing I reduces the degrees of freedom in the transport problem by D per mode, improving identifiability (Statement 1, §2).

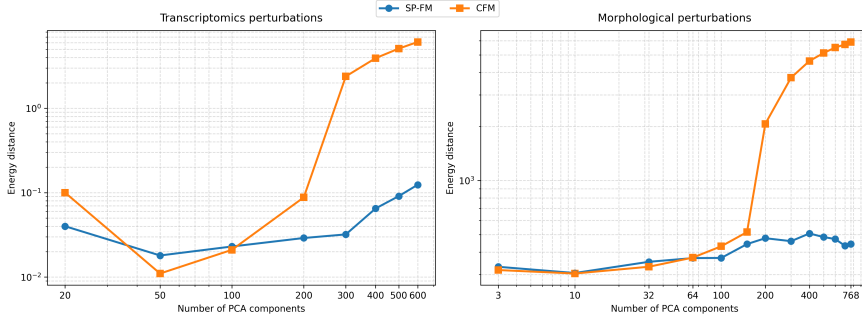
Robustness to data dimensionality. A known challenge for flow-based models is scaling to high-dimensional spaces, where the fixed Gaussian base distribution $\mathcal{N}(0, I)$ becomes increasingly mismatched to structured target distributions. We investigate this by training both SP-FM and CFM on PCA-reduced representations with increasing numbers of components. Figure 3b shows that CFM’s performance degrades substantially as dimensionality increases: the energy

Table 4: BBBC021 and RxRx1 benchmarks comparing SP-FM and CFM on phenotypic perturbations. Lower is better; values are the mean over three runs.

Dataset	Model	MMD \downarrow	W1 \downarrow	W2 \downarrow	ED \downarrow
BBBC021	CFM	0.2504 \pm 0.001	108.4093 \pm 0.291	5903.8647 \pm 32.33	18.9197 \pm 0.088
	SP-FM	0.0439 \pm 0.002	29.4752 \pm 0.733	442.9421 \pm 24.11	2.4036 \pm 0.087
RxRx1	CFM	0.2527 \pm 0.001	118.7191 \pm 1.23	7077.8330 \pm 43.21	20.5810 \pm 0.31
	SP-FM	0.0307 \pm 0.001	30.8660 \pm 0.12	483.2796 \pm 4.69	1.6731 \pm 0.034



(a) Energy distance versus number of GMM modes on transcriptomic (left) and morphological (right) datasets. Performance improves with more modes up to a dataset-dependent optimum.



(b) Energy distance versus PCA dimensionality for SP-FM and CFM. SP-FM maintains stable performance while CFM degrades in higher dimensions.

Figure 3: **Ablation studies** on transcriptomic (Combo-SciPlex) and morphological (BBBC021) datasets. (a) Effect of the number of GMM modes on generation quality. (b) Comparison of SP-FM and CFM robustness across increasing data dimensionality.

distance grows by over an order of magnitude between 50 and 500 PCA components. In contrast, SP-FM maintains stable performance across the full range of dimensionalities tested. This robustness arises because the learned GMM base distribution adapts to the structure of each condition, reducing the effective transport distance even in high dimensions. From the perspective of Section 4, higher D increases the constraint count ($ID + I$), which for fixed I reduces the residual degrees of freedom $J - ID$, explaining why SP-FM’s advantage becomes more pronounced in higher dimensions.

These ablations confirm two key properties of SP-FM: (i) the number of mixture components provides a useful complexity knob that should be tuned to dataset heterogeneity, and (ii) conditioning the base distribution yields substantial robustness benefits in high-dimensional settings where standard CFM struggles.

7 Limitations and Future Work

While SP-FM demonstrates strong performance across diverse perturbation modalities, several limitations remain. The framework depends on the availability of high-quality perturbation descriptors such as gene embeddings or chemical fingerprints; incomplete or noisy metadata may hinder predictive accuracy. Our evaluation focuses primarily on single perturbations and small combinations, whereas scaling to higher-order combinations, dose-response landscapes, and time-course dynamics remains an open challenge. Moreover, although we provide theoretical justification for out-of-distribution generalisation, the analysis assumes smooth transport fields that may not fully capture heterogeneous tissues or disease states.

Future work should address these challenges by incorporating richer multimodal descriptors, extending the model to capture interaction effects and temporal responses, and scaling training to very large datasets. In particular, applying SP-FM to resources such as the JUMP- consortium dataset for imaging assays [Chandrasekaran et al., 2024] and large single-cell perturbation compendia [Zhang et al., 2025a] could enable the development of true zero-shot models that leverage perturbation similarity at scale. Finally, extending the framework to translational settings such as patient-derived cells or organoids will be critical for realising its potential impact in therapeutic design.

Acknowledgments

This work is supported by Open Targets (Drug2Cell) and by the Chan Zuckerberg Initiative DAF Single-Cell Biology Data Insights program.

Conflict of interest

M.L. has equity interests in Relation Therapeutics, is a scientific co-founder and part-time employee of AIVIVO, and serves on the scientific advisory board of Novo Nordisk.

Code availability

Code is publicly available on github: <https://github.com/Lotfollahi-lab/MixFlow>.

References

Abhinav K. Adduri, Dhruv Gautam, Beatrice Bevilacqua, Alishba Imran, Rohan Shah, Mohsen Naghipourfar, Noam Teyssier, Rajesh Ilango, Sanjay Nagaraj, Mingze Dong, Chiara Ricci-Tam, Christopher Carpenter, Vishvak Subramanyam, Aidan Winters, Sravya Tirukkoveri, Jeremy Sullivan, Brian S. Plosky, Basak Eraslan, Nicholas D. Youngblut, Jure Leskovec, Luke A. Gilbert, Silvana Konermann, Patrick D. Hsu, Alexander Dobin, Dave P. Burke, Hani Goodarzi, and Yusuf H. Roohani. Predicting cellular responses to perturbation across diverse contexts with STATE. *bioRxiv*, 2025. doi: 10.1101/2025.06.26.661135. URL <https://doi.org/10.1101/2025.06.26.661135>. preprint.

Md Atik Ahamed, Qiang Ye, and Qiang Cheng. Molsnap: Snap-fast molecular generation with latent variational mean flow. *arXiv preprint arXiv:2508.05411*, 2025. doi: 10.48550/arXiv.2508.05411. URL <https://arxiv.org/abs/2508.05411>.

Constantin Ahlmann-Eltze, Wolfgang Huber, and Simon Anders. Deep-learning-based gene perturbation effect prediction does not yet outperform simple linear baselines. *Nature Methods*, 22:1657–1661, 2025. doi: 10.1038/s41592-025-02772-6. URL <https://doi.org/10.1038/s41592-025-02772-6>.

Lazar Atanackovic, Xi Zhang, Brandon Amos, Mathieu Blanchette, Leo J. Lee, Yoshua Bengio, Alexander Tong, and Kirill Neklyudov. Meta flow matching: Integrating vector fields on the wasserstein manifold. 2024.

Jacob Bamberger, Iolo Jones, Dennis Duncan, Michael M Bronstein, Pierre Vandergheynst, and Adam Gosztolai. Carr\’e du champ flow matching: better quality-generalisation tradeoff in generative models. *arXiv preprint arXiv:2510.05930*, 2025.

Jean-David Benamou and Yann Brenier. A computational fluid mechanics solution to the monge-kantorovich mass transfer problem. *Numerische Mathematik*, 84(3):375–393, 2000.

Michael Bereket and Theofanis Karaletsos. Modelling cellular perturbations with the sparse additive mechanism shift variational autoencoder. *Advances in Neural Information Processing Systems*, 36:1–12, 2023.

Quentin Bertrand, Anne Gagneux, Mathurin Massias, and Rémi Emonet. On the closed-form of flow matching: Generalization does not arise from target stochasticity. *arXiv preprint arXiv:2506.03719*, 2025.

Xin Bing, Florentina Bunea, and Jonathan Niles-Weed. Estimation and inference for the wasserstein distance between mixing measures in topic models. *arXiv preprint arXiv:2206.12768*, 2022.

Mark-Anthony Bray, Shantanu Singh, Han Han, Chadwick T Davis, Blake Borgeson, Cathy Hartland, Maria Kost-Alimova, Sigrun M Gustafsdottir, Christopher C Gibson, and Anne E Carpenter. Cell painting, a high-content image-based assay for morphological profiling using multiplexed fluorescent dyes. *Nature protocols*, 11(9):1757–1774, 2016.

Charlotte Bunne, Stefan G Stark, Gabriele Gut, Jacobo Sarabia Del Castillo, Mitch Levesque, Kjong-Van Lehmann, Lucas Pelkmans, Andreas Krause, and Gunnar Rätsch. Learning single-cell perturbation responses using neural optimal transport. *Nature methods*, 20(11):1759–1768, 2023.

Peter D. Caie, Rebecca E. Walls, Alexandra Ingleston-Orme, Sandeep Daya, Tom Houslay, Rob Eagle, Mark E. Roberts, and Neil O. Carragher. High-content phenotypic profiling of drug response signatures across distinct cancer cells. *Molecular Cancer Therapeutics*, 9(6):1913–1926, 2010. doi: 10.1158/1535-7163.MCT-09-1148. URL <https://aacrjournals.org/mct/article/9/6/1913/93798/High-Content-Phenotypic-Profiling-of-Drug-Response>.

Srinivas Niranj Chandrasekaran, Beth A Cimini, Amy Goodale, Lisa Miller, Maria Kost-Alimova, Nasim Jamali, John G Doench, Briana Fritchman, Adam Skepner, Michelle Melanson, et al. Three million images and morphological profiles of cells treated with matched chemical and genetic perturbations. *Nature Methods*, 21(6):1114–1121, 2024.

Hansheng Chen, Kai Zhang, Hao Tan, Zexiang Xu, Fujun Luan, Leonidas Guibas, Gordon Wetzstein, and Sai Bi. Gaussian mixture flow matching models. *arXiv preprint arXiv:2504.05304*, 2025. doi: 10.48550/arXiv.2504.05304. URL <https://arxiv.org/abs/2504.05304>.

Julie Delon and Agnes Desolneux. A wasserstein-type distance in the space of gaussian mixture models. *SIAM Journal on Imaging Sciences*, 13(2):936–970, 2020.

Leon Hetzel, Simon Boehm, Niki Kilbertus, Stephan Günnemann, Fabian Theis, et al. Predicting cellular responses to novel drug perturbations at a single-cell resolution. *Advances in Neural Information Processing Systems*, 35: 26711–26722, 2022.

Jonathan Ho and Tim Salimans. Classifier-free diffusion guidance. In *NeurIPS 2021 Workshop on Deep Generative Models and Downstream Applications*, 2021.

Dominik Klein, Jonas Simon Fleck, Daniil Bobrovskiy, Lea Zimmermann, Sören Becker, Alessandro Palma, Leander Dony, Alejandro Tejada-Lapuerta, Guillaume Huguet, Hsiu-Chuan Lin, Nadezhda Azbukina, Fátima Sanchís-Calleja, Theo Uscidda, Artur Szalata, Manuel Gander, Aviv Regev, Barbara Treutlein, J. Gray Camp, and Fabian J. Theis. Cellflow enables generative single-cell phenotype modeling with flow matching. *bioRxiv*, 2025. doi: 10.1101/2025.04.11.648220. URL <https://doi.org/10.1101/2025.04.11.648220>. preprint.

Yaron Lipman, Ricky T. Q. Chen, Heli Ben-Hamu, Maximilian Nickel, and Matthew Le. Flow matching for generative modeling. In *International Conference on Learning Representations (ICLR)*, 2022. URL <https://openreview.net/forum?id=PQqzTYqlLx>.

Mohammad Lotfollahi, Anna Klimovskaia Susmelj, Carlo De Donno, Leon Hetzel, Yuge Ji, Ignacio L Ibarra, Sanjay R Srivatsan, Mohsen Naghipourfar, Riza M Daza, Beth Martin, et al. Predicting cellular responses to complex perturbations in high-throughput screens. *Molecular systems biology*, 19(6):e11517, 2023.

Zeinab Navidi, Jun Ma, Esteban A Miglietta, Le Liu, Anne E Carpenter, Beth A Cimini, Benjamin Haibe-Kains, and Bo Wang. Morphodiff: Cellular morphology painting with diffusion models. *bioRxiv*, 2024.

Viet-Anh Nguyen. Approximation of probability density functions by gaussian mixtures in wasserstein distance. *Journal of Mathematical Analysis and Applications*, 475(2):1750–1772, 2019.

Thomas M. Norman, Max Horlbeck, Jesse M. Replogle, Alexander Y. Ge, Alanna Xu, Mengmeng Jost, Luke A. Gilbert, Emily A. Weissman, Jonathan S. Chen, Matthew A. Cortez, David A. Weissman, Andrew P. Schoenfeld, Neville E. R. Sanjana, and Jonathan S. Weissman. Exploring genetic interaction manifolds constructed from rich single-cell phenotypes. *Science*, 365(6455):786–793, 2019. doi: 10.1126/science.aax4438.

Maxime Oquab, Timothée Darcet, Théo Moutakanni, Huy Vo, Marc Szafraniec, Vasil Khalidov, Pierre Fernandez, Daniel Haziza, Francisco Massa, Alaaeldin El-Nouby, Mahmoud Assran, Nicolas Ballas, Wojciech Galuba, Russell Howes, Po-Yao Huang, Shang-Wen Li, Ishan Misra, Michael Rabbat, Vasu Sharma, Gabriel Synnaeve, Hu Xu, Hervé Jegou, Julien Mairal, Patrick Labatut, Armand Joulin, and Piotr Bojanowski. Dinov2: Learning robust visual features without supervision, 2024. URL <https://arxiv.org/abs/2304.07193>.

A. Palma, F. J. Theis, and M. Lotfollahi. Predicting cell morphological responses to perturbations using generative modeling. *Nature Communications*, 16:505, 2025. doi: 10.1038/s41467-024-55707-8. URL <https://doi.org/10.1038/s41467-024-55707-8>.

Gabriel Peyré, Marco Cuturi, et al. Computational optimal transport: With applications to data science. *Foundations and Trends® in Machine Learning*, 11(5-6):355–607, 2019.

Joseph M. Replogle, Reuben A. Saunders, Angela N. Pogson, Jeffrey A. Hussmann, Alexander Lenail, Alina Guna, Lauren Mascibroda, Eric J. Wagner, Karen Adelman, Gila Lithwick-Yanai, Nika Iremadze, Florian Oberstrass, Doron Lipson, Jessica L. Bonnar, Marco Jost, Thomas M. Norman, and Jonathan S. Weissman. Mapping information-rich genotype-phenotype landscapes with genome-scale perturb-seq. *Cell*, 185(14):2559–2575.e28, 2022. ISSN 0092-8674. doi: 10.1016/j.cell.2022.05.013. URL <https://www.sciencedirect.com/science/article/pii/S0092867422005979>.

David Rogers and Mathew Hahn. Extended-connectivity fingerprints. *Journal of Chemical Information and Modeling*, 50(5):742–754, 2010. doi: 10.1021/ci100050t.

Robin Rombach, Andreas Blattmann, Dominik Lorenz, Patrick Esser, and Björn Ommer. High-resolution image synthesis with latent diffusion models, 2022. URL <https://arxiv.org/abs/2112.10752>.

Yusuf Roohani, Kexin Huang, and Jure Leskovec. Predicting transcriptional outcomes of novel multigene perturbations with gears. *Nature Biotechnology*, 42(6):927–935, 2024.

M. Schubert et al. Perturb-seq: Dissecting molecular circuits with scalable single-cell rna profiling of pooled genetic screens. *Nature Methods*, 15:941–945, 2018.

Yang Song and Stefano Ermon. Generative modeling by estimating gradients of the data distribution. *Advances in neural information processing systems*, 32, 2019.

Sanjay R Srivatsan, José L McFaline-Figueroa, Vijay Ramani, Lauren Saunders, Junyue Cao, Jonathan Packer, Hannah A Pliner, Dana L Jackson, Riza M Daza, Lena Christiansen, et al. Massively multiplex chemical transcriptomics at single-cell resolution. *Science*, 367(6473):45–51, 2020.

Aravind Subramanian, Rajiv Narayan, Steven M Corsello, David D Peck, Ted E Natoli, Xiaodong Lu, Joshua Gould, John F Davis, Andrew A Tubelli, Jacob K Asiedu, et al. A next generation connectivity map: L1000 platform and the first 1,000,000 profiles. *Cell*, 171(6):1437–1452, 2017.

Maciej Sypetkowski, Morteza Rezanejad, Saber Saberian, Oren Kraus, John Urbanik, James Taylor, Ben Mabey, Mason Victors, Jason Yosinski, Alborz Rezazadeh Sereshkeh, Imran Haque, and Berton Earnshaw. Rxrx1: A dataset for evaluating experimental batch correction methods, 2023. URL <https://arxiv.org/abs/2301.05768>.

Alexander Tong, Kilian Fatras, Nikolay Malkin, Guillaume Huguet, Yanlei Zhang, Jarrid Rector-Brooks, Guy Wolf, and Yoshua Bengio. Improving and generalizing flow-based generative models with minibatch optimal transport. *arXiv preprint arXiv:2302.00482*, 2023.

Z. Wang, N. R. Clark, and A. Ma’ayan. Crowdsourcing a drug connectivity map. *Nature Reviews Drug Discovery*, 15: 718–729, 2016.

TaeHo Yoon, Joo Young Choi, Sehyun Kwon, and Ernest K Ryu. Diffusion probabilistic models generalize when they fail to memorize. In *ICML 2023 workshop on structured probabilistic inference {\&} generative modeling*, 2023.

Jesse Zhang, Airol A Ubas, Richard de Borja, Valentine Svensson, Nicole Thomas, Neha Thakar, Ian Lai, Aidan Winters, Umair Khan, Matthew G Jones, et al. Tahoe-100m: A giga-scale single-cell perturbation atlas for context-dependent gene function and cellular modeling. *BioRxiv*, pages 2025–02, 2025a.

Richard Zhang, Phillip Isola, Alexei A. Efros, Eli Shechtman, and Oliver Wang. The unreasonable effectiveness of deep features as a perceptual metric, 2018. URL <https://arxiv.org/abs/1801.03924>.

Yuhui Zhang, Yuchang Su, Chenyu Wang, Tianhong Li, Zoe Wefers, Jeffrey Nirschl, James Burgess, Daisy Ding, Alejandro Lozano, Emma Lundberg, and Serena Yeung-Levy. Cellflux: Simulating cellular morphology changes via flow matching. *arXiv preprint arXiv:2502.09775*, 2025b. doi: 10.48550/arXiv.2502.09775. URL <https://arxiv.org/abs/2502.09775>.

Qijia Zheng and Kai Tang. Universal approximation of probability distributions by gaussian mixture models. *Neural Computation*, 32(4):829–848, 2020.

A Generalisation analysis, details and proofs

As outlined in Sec. 4, to circumvent the infinite-dimensional Wasserstein manifold of measures and to enable the adoption of theoretical generalization guarantees for finite-dimensional spaces, we assume that the target distribution ρ is itself a Gaussian mixture model (GMM) with J components, fixed mode locations that cover \mathbb{R}^D as $J \rightarrow \infty$, and varying mixture weights. Moreover, recall that μ and ρ denote the base and target distributions, respectively.

Definition 2 (Mixture Wasserstein Distance). *Let $\mu_{GMM(\Theta, p)}$ and $\rho_{GMM(\Gamma, q)}$ be two measures induced by their corresponding GMMs with I and J modes, mode positions $\Theta \in \mathbb{R}^{I \times D}$ and $\Gamma \in \mathbb{R}^{J \times D}$, and mode weights $p \in \mathbb{S}^{I-1}$ and $q \in \mathbb{S}^{J-1}$. The mixture Wasserstein distance between $\mu_{GMM(\Theta, p)}$ and $\rho_{GMM(\Gamma, q)}$ is defined as follows:*

$$\mathcal{MW}_2^2(\mu, \rho) = \inf_{V \in \mathbb{R}^{I \times J}} \sum_{i=1}^I \sum_{j=1}^J \|\Theta_i - \Gamma_j\|_2^2 v_{ij} p_i \quad (8)$$

$$\text{s.t. } \sum_{j=1}^J v_{ij} = 1 \quad , \quad \forall i \in \{1, \dots, I\} \quad (9)$$

$$q_j = \sum_{i=1}^I v_{ij} p_i \quad , \quad \forall j \in \{1, \dots, J\} \quad (\text{boundary condition}) \quad (10)$$

$$v_{ij} \geq 0 \quad , \quad \forall i \in \{1, \dots, I\}, \forall j \in \{1, \dots, J\} \quad (11)$$

This is equivalent to discrete optimal transport between the GMMs' modes with the transportation cost determined by their mode locations. Intuitively, v_{ij} is the portion of mass of the i -th mode in the 1st GMM μ which is moved to the j -th mode in the 2nd GMM ρ .

Definition 3 (Mixture Wasserstein Flow). *The matrix $V^{I \times J}$ in Eq. 8 induces a time-dependant flow $v : \mathbb{R}^D \times [0, 1] \rightarrow \mathbb{R}^D$ referred to as mixture Wasserstein flow.*

Lemma 4 (Dual of Mixture Wasserstein Distance). *The dual form of the constrained optimisation of Eq. 8 is as follows:*

$$\sup_{z \in \mathbb{R}^{I+J}} \sum_{i=1}^I z_i + \sum_{j=1}^J q_j z_{j+I} \quad (12)$$

$$\text{s.t. } z_i + p_i \cdot z_{j+I} \leq p_i \|\Theta_i - \Gamma_j\|_2^2 \quad , \quad \forall i \in \{1, \dots, I\}, j \in \{1, \dots, J\} \quad (13)$$

$$\{z_1, z_2, \dots, z_{I+J}\} \text{ unrestricted in sign, i.e. } \in \mathbb{R} \quad (14)$$

Definition 5 (Subset sum condition). *In the discrete optimal transport problem of Eq. 8, the marginal measures $[p_1, \dots, p_I]$ and $[q_1, \dots, q_J]$ are said to meet the subset sum condition if for any proper non-empty subsets of them - denoted by $\{p_{i_1}, \dots, p_{i_{I'}}\}$ and $\{q_{j_1}, \dots, q_{j_{J'}}\}$ - we have that*

$$(p_{i_1} + \dots + p_{i_{I'}}) \neq (q_{j_1} + \dots + q_{j_{J'}}). \quad (15)$$

Statement 6. *In the discrete optimal transport problem of Eq. 8 assume that the marginal distributions meet the subset sum condition. Then we have that:*

1. Any optimal solution of Eq. 8, $V^* \in \mathbb{R}^{I \times J}$, has exactly $I + J - 1$ non-zero elements.
2. A dual constraint in Eq. 13 is binding if and only if the corresponding $V^*[i, j] = v_{ij}^*$ is non-zero.
3. The dual problem of Eq. 12 has a unique optimum $z^* \in \mathbb{R}^{I+J}$.

The importance of Statement 6 is that - as we will prove in Statement 8 - for any μ and ρ the subset sum condition, and hence 1, 2, and 3 explained above hold almost surely. Therefore, we can generally assume 1, 2, and 3 in Statement 6 hold for any μ and ρ .

Statement 7. *In the discrete optimal transport problem of Eq. 8 assume that the marginal distributions meet the subset sum condition. Moreover, assume that Θ , Γ , p , and $[z_1^*, \dots, z_I^*]$ in the dual form are known and fixed. Then $V_{\geq 0}^*$ is uniquely determined, where $V^* \in \mathbb{R}^{I \times J}$ is an optimal solution for Eq. 8, and $V_{\geq 0}^* \in \mathbb{R}^{I \times J}$ is a matrix where the element in its i -th row and j -th column is 1 if $v_{ij}^* > 0$ and is 0 otherwise.*

Proof: The constraint of Eq. 12 rewrites as

$$z_{j+I} \leq \left[\|\Theta_i - \Gamma_j\|_2^2 - \frac{z_i}{p_i} \right] \quad (16)$$

To maximise the objective of Eq. 12, the variables z_{j+I} should take their maximum possible value. Therefore we have that

$$z_{j+I}^* = \max_{1 \leq i \leq I} \left[\|\Theta_i - \Gamma_j\|_2^2 - \frac{z_i^*}{p_i} \right]. \quad (17)$$

In other words, given $[z_1^*, \dots, z_I^*]$ the above equation uniquely specifies the values for $[z_{I+1}^*, \dots, z_{I+J}^*]$ and regardless of the probability values of the target distribution $\mathbf{q} \in \mathbb{R}^J$. According to Statement 6, in Eq. 17 equality holds if and only if $v_{ij}^* > 0$, and this determines $\mathbf{V}_{\geq 0}^*$. ■

The importance of Statement 7 is that, intuitively, having predicted the closest GMM to ρ (i.e. Θ and \mathbf{p}), having predicted the first I optimal dual values $[z_1^*, \dots, z_I^*] \in \mathbb{R}^I$, and having fixed the GMM modes that cover the feature space (i.e. Γ), $\mathbf{V}_{\geq 0}^*$ is uniquely identified. This is important, because to obtain a predictor $\mathbf{V}_{\geq 0}^* \approx h_{\mathbf{V}_{\geq 0}^*}(\mathbf{y})$ where $h_{\mathbf{V}_{\geq 0}^*} : \mathbb{R}^{\dim(\mathbf{y})} \rightarrow \{0, 1\}^{I \times J}$, one can instead train the following three predictors, and $h_{\mathbf{V}_{\geq 0}^*}(\cdot)$ will be uniquely determined:

1. $\Theta \approx h_{\Theta}(\mathbf{y})$, where $h_{\Theta} : \mathbb{R}^{\dim(\mathbf{y})} \rightarrow \mathbb{R}^{I \times D}$.
2. $\mathbf{p} \approx h_{\mathbf{p}}(\mathbf{y})$, where $h_{\mathbf{p}} : \mathbb{R}^{\dim(\mathbf{y})} \rightarrow \mathbb{S}^{I-1}$.
3. $[z_1^*, \dots, z_I^*] \approx h_z(\mathbf{y})$, where $h_z : \mathbb{R}^{\dim(\mathbf{y})} \rightarrow \mathbb{R}^I$

Statement 8. Let $\mu_{GMM(\Theta, \mathbf{p})}$ and $\rho_{GMM(\Gamma, \mathbf{q})}$ be two measures induced by their corresponding GMMs. Then the marginal distributions \mathbf{p} and \mathbf{q} meet the subset sum condition almost surely. Therefore, Statements 6 and 7 hold almost surely.

Proof: There are $(2^I - 2) \times (2^J - 2)$ pairs of proper non-empty subsets from the marginal measures $[p_1, \dots, p_I]$ and $[q_1, \dots, q_J]$. Each such a pair like $\{p_{i1}, \dots, p_{iI'}\}$ and $\{q_{j1}, \dots, q_{jJ'}\}$ specify the following subspace of $\mathbb{S}^{I-1} \times \mathbb{S}^{J-1}$ where the subset sum condition is violated:

$$p_{i1} + \dots + p_{iI'} = q_{j1} + \dots + q_{jJ'} \quad (18)$$

Each such subspace has zero measure, so the union of these $(2^I - 2) \times (2^J - 2)$ subspaces has also zero measure. ■

Definition 9 (Projection to subspace of GMMs with I modes). Let $\rho_{GMM(\Gamma, \mathbf{q})}$ be a measure induced by a GMM with modes $\Gamma \in \mathbb{R}^{J \times D}$ and mode probabilities $\mathbf{q} \in \mathbb{S}^{J-1}$. The goal is to find the closest measure to $\rho_{GMM(\Gamma, \mathbf{q})}$ which is induced by a GMM with I modes, where $I \ll J$ and in terms of mixture Wasserstein distance. This GMM $\mu_{GMM(\Theta^*, \mathbf{p}^*)}$ is found by:

$$\Theta^*, \mathbf{p}^* = \underset{\substack{\Theta \in \mathbb{R}^{I \times D} \\ \mathbf{p} \in \mathbb{R}^I}}{\operatorname{argmin}} \mathcal{MW}_2^2(\mu_{GMM(\Theta, \mathbf{p})}, \rho_{GMM(\Gamma, \mathbf{q})}) \quad (19)$$

Let's assume we have the 3 predictors $h_{\Theta}(\cdot)$, $h_{\mathbf{p}}(\cdot)$, and $h_z(\cdot)$ explained above, that take in the population descriptor \mathbf{y} and predict the projection of the unseen ρ to the space of GMMs (i.e. Θ^* and \mathbf{p}^*) as well the I dual solution values $[z_1^*, \dots, z_I^*]$. Given these, according to Statement 7 we can uniquely determine $I + J - 1$ elements of $\mathbf{V}^* \in \mathbb{R}^{I \times J}$ which are non-zero, and the rest are uniquely set to zero. Recall that the goal is to predict the flow $\mathbf{V}^* \in \mathbb{R}^{I \times J}$, because when it is applied to the measure $\mu_{GMM(\Theta^*, \mathbf{p}^*)}$ it gives us the prediction for ρ . Having identified non-zero elements of \mathbf{V}^* , Statements 10 and 11 impose linear constraints on the identified elements, thereby improving the identification and prediction of \mathbf{V}^* .

Statement 10 (Barycentre condition). For the matrix $\Theta^* \in \mathbb{R}^{I \times D}$ in Eq. 19 we have that

$$\Theta_i^* = \sum_{j=1}^J v_{ij}^* \Gamma_j. \quad (20)$$

Proof: We compute the derivative of Eq. 8 with respect to Θ_i and set it to zero:

$$\frac{\partial}{\partial \Theta_i} \sum_{j=1}^J \|\Theta_i - \Gamma_j\|_2^2 v_{ij}^* p_i = \quad (21)$$

$$\frac{\partial}{\partial \Theta_i} \sum_{j=1}^J [\Theta_i^T \Theta_i - 2\Theta_i^T \Gamma_j] v_{ij}^* p_i = \quad (22)$$

$$\sum_{j=1}^J [2\Theta_i - 2\Gamma_j] v_{ij}^* p_i = \quad (23)$$

$$2p_i \left[\Theta_i \sum_{j=1}^J v_{ij}^* - \sum_{j=1}^J v_{ij}^* \Gamma_j \right] = 0 \quad (24)$$

$$\Rightarrow \Theta_i^* = \sum_{j=1}^J v_{ij}^* \Gamma_j \quad (25)$$

■

Statement 11 (Optimality condition for mode probabilities). *The following optimality condition*

$$\frac{\partial}{\partial \mathbf{p}} \mathcal{MW}_2^2(\mu_{GMM}(\Theta^*, \mathbf{p}), \rho_{GMM}(\Gamma, \mathbf{q}))|_{\mathbf{p}=\mathbf{p}^*} = 0 \quad (26)$$

implies that

$$\sum_{j=1}^J v_{ij}^* \|\Theta_i^* - \Gamma_j\|_2^2 = \text{const}, \quad \forall i \in \{1, \dots, I\}. \quad (27)$$

Proof: At the optimal point $[\Theta^*, \mathbf{p}^*]$, if two mode probabilities like $p_{i_1}^*$ and $p_{i_2}^*$ are changed by $+\epsilon$ and $-\epsilon$ (where ϵ is a small positive scalar), we have that

$$\frac{\text{change in } \mathcal{MW}_2^2}{\text{change in } \mathbf{p}} \quad (28)$$

$$= \frac{1}{\epsilon} \left[\sum_{j=1}^J \|\Theta_{i_1}^* - \Gamma_j\|_2^2 v_{i_1 j}^* (+\epsilon) \right] + \frac{1}{\epsilon} \left[\sum_{j=1}^J \|\Theta_{i_2}^* - \Gamma_j\|_2^2 v_{i_2 j}^* (-\epsilon) \right] \quad (29)$$

$$= \left[\sum_{j=1}^J \|\Theta_{i_1}^* - \Gamma_j\|_2^2 v_{i_1 j}^* \right] - \left[\sum_{j=1}^J \|\Theta_{i_2}^* - \Gamma_j\|_2^2 v_{i_2 j}^* \right] = 0 \quad (30)$$

Therefore

$$\sum_{j=1}^J \|\Theta_{i_1}^* - \Gamma_j\|_2^2 v_{i_1 j}^* = \sum_{j=1}^J \|\Theta_{i_2}^* - \Gamma_j\|_2^2 v_{i_2 j}^* \quad \forall i_1, i_2 \in \{1, \dots, I\}, \quad i_1 \neq i_2. \quad (31)$$

■

Now we are ready to state the training phase and testing phase of the learning algorithm.

Statement 12 (Training phase). *Given is a set of N GMM-induced measures $\{\rho_{GMM}(\Gamma, \mathbf{q}^{(n)})\}_{n=1}^N$ and their corresponding population descriptors $\{\mathbf{y}_1, \dots, \mathbf{y}_N\}$. Note that the matrix $\Gamma \in \mathbb{R}^{J \times D}$ are the GMM modes in the target distribution that carpet the feature space, and are kept fixed during training and testing, hence to superscript n for Γ . For each dataset instance, the following vectors and matrices are obtained*

1. The parameters of the closest GMM to $\rho_{GMM}(\Gamma, \mathbf{q}^{(n)})$ and with I modes:

$$\Theta^{*(n)}, \mathbf{p}^{*(n)} = \underset{\substack{\Theta \in \mathbb{R}^{I \times D} \\ \mathbf{p} \in \mathbb{R}^I}}{\operatorname{argmin}} \mathcal{MW}_2^2(\mu_{GMM}(\Theta, \mathbf{p}), \rho_{GMM}(\Gamma, \mathbf{q}^{(n)})) \quad (32)$$

2. Having obtained $\Theta^{*(n)}$ and $\mathbf{p}^{*(n)}$, solve the dual form of Eq. 12 for the distributions $\mu_{GMM}(\Theta^{*(n)}, \mathbf{p}^{*(n)})$ and $\rho_{GMM}(\Gamma^{(n)}, \mathbf{q}^{(n)})$. Save the first I elements of the dual solution $[z_1^{*(n)}, \dots, z_I^{*(n)}]$.

Now having obtained $\{\Theta^{*(n)}, \mathbf{p}^{*(n)}, [z_1^{*(n)}, \dots, z_I^{*(n)}]\}_{n=1}^N$, the following predictors are trained

1. $\Theta^{*(n)} \approx h_{\Theta}(\mathbf{y}_n)$, where $h_{\Theta} : \mathbb{R}^{\dim(\mathbf{y})} \rightarrow \mathbb{R}^{I \times D}$.
2. $\mathbf{p}^{*(n)} \approx h_{\mathbf{p}}(\mathbf{y}_n)$, where $h_{\mathbf{p}} : \mathbb{R}^{\dim(\mathbf{y})} \rightarrow \mathbb{S}^{I-1}$.
3. $[z_1^{*(n)}, \dots, z_I^{*(n)}] \approx h_z(\mathbf{y}_n)$, where $h_z : \mathbb{R}^{\dim(\mathbf{y})} \rightarrow \mathbb{R}^I$

Statement 13 (Testing phase). *In the testing phase, a population descriptor \mathbf{y}_{test} is given. Firstly, the following vectors/matrices are predicted:*

1. $\Theta^{(test)} \approx h_{\Theta}(\mathbf{y}_{test})$.
2. $\mathbf{p}^{(test)} \approx h_{\mathbf{p}}(\mathbf{y}_{test})$
3. $[z_1^{(test)}, \dots, z_I^{(test)}] \approx h_z(\mathbf{y}_{test})$

Now having obtained $[\Theta^{(test)}, \mathbf{p}^{(test)}, [z_1^{(test)}, \dots, z_I^{(test)}]]$, according to Statement 7 $\mathbf{V}_{\geq 0}^{test}$ is uniquely identified and according to Statement 8 almost surely has exactly $I + J - 1$ non-zero elements. In other words, at this point we are left with $I + J - 1$ variables (i.e. v_{ij}^{test} -s) that we want to identify as closely as possible. For these $I + J - 1$ variables, we have the following constraints

1. Each barycentre condition in Eq. 20 provides D linear constraints on non-zero v_{ij}^{test} -s, resulting in $I \times D$ linear constraints. Note that the matrix $\Gamma \in \mathbb{R}^{J \times D}$ are the GMM modes in the target distribution that carpet the feature space, and are kept fixed throughout.
2. Each constraint of Eq. 27 provides a linear constraint, resulting in I more linear constraints. We add the constant scalar in Eq. 27 to our variable list, so we have $I + J$ variables to identify.

In sum, we have $I + J$ variables, $ID + I$ constraints, and hence $J - ID$ degrees of freedom. Having estimated $\Theta^{(test)}$ and the flow $\mathbf{V}^{(test)}$, we can apply the latter on the former to arrive at an estimate for $\rho^{(test)}$

Statement 14. If $I = 1$ the dual problem of Eq. 12 is ill-defined. **Proof:** If $I = 1$, according to Eq. 17, we have that

$$z_{j+I}^* = \|\Theta_1 - \Gamma_j\|_2^2 - \frac{z_1^*}{p_1} \quad (33)$$

If we substitute this in Eq. 12

$$\sup_{\mathbf{z} \in \mathbb{R}^{1+J}} z_1 + \sum_{j=1}^J q_j z_{j+I} = \quad (34)$$

$$\sup_{\mathbf{z} \in \mathbb{R}^{1+J}} z_1 + \sum_{j=1}^J q_j \left[\|\Theta_1 - \Gamma_j\|_2^2 - \frac{z_1}{p_1} \right]_1 = \quad (35)$$

$$\sup_{\mathbf{z} \in \mathbb{R}^{1+J}} z_1 - z_1 \sum_{j=1}^J q_j + \sum_{j=1}^J q_j \left[\|\Theta_1 - \Gamma_j\|_2^2 \right] \quad (36)$$

In the last equation z_1 is cancelled out from the objective. ■

Essentially, according to Statement 14 the described training and testing procedure fail, and this discourages the use of uni-modal Gaussian distribution as the base distribution.

B Letters

B.1 Dataset details

B.2 Synthetic Letters Dataset (Letter–Rotation Benchmark)

Data generation. We construct a synthetic benchmark by rendering uppercase letters as binary silhouettes and sampling point clouds from the foreground pixels. Each condition corresponds to a (letter, rotation) pair. For a given letter, we generate $R = 20$ rotations uniformly spaced in $[0, 2\pi]$. For each condition, we create multiple replicas by rendering the same silhouette with different RGB colours; these replicas are used only to provide multiple samples from the same conditional distribution and are not included in the conditioning vector.

Point-cloud representation. Each sample is a point cloud in \mathbb{R}^D with $D = 5$, consisting of 2D coordinates and RGB channels: $\mathbf{x} = (x, y, r, g, b)$. We extract foreground-pixel coordinates, normalize them to $[-1, 1]^2$, rescale to correct aspect ratio using the glyph’s bounding box, optionally add Gaussian coordinate noise (set to 0 in our experiments), and finally rotate the point cloud by the condition’s angle.

Colour replicas. For each (letter, rotation) condition, we generate C colour replicas to better approximate the underlying conditional distribution. In our experiments we use $C = 100$. To ensure that colour does not dominate the evaluation metrics, we restrict the colour variation to a narrow range by sampling only the red channel $r \sim \text{Unif}(r_{\min}, r_{\max})$ with $(r_{\min}, r_{\max}) = (0.5, 0.6)$ and setting $g = b = 0$; thus colour provides mild diversity without strongly affecting distance metrics.

Condition descriptor. The conditioning vector \mathbf{y} concatenates (i) a one-hot encoding of the letter identity and (ii) a continuous rotation scalar normalized to $[0, 1]$:

$$\mathbf{y} = [\text{onehot}(\text{letter}); \theta/(2\pi)].$$

Colour is not included in \mathbf{y} .

Source distribution. For conditional flow-matching training we sample the source point cloud from an isotropic Gaussian. In the our setting, each source point cloud uses a shared RGB value across all points (sampled uniformly within the same restricted colour range) while the 2D coordinates are sampled from $\mathcal{N}(0, I)$, matching the data format of the target clouds.

Train/validation/test splits (rotation interpolation). We study rotation interpolation by splitting the rotation indices: training uses even-indexed rotations, while validation and test use odd-indexed rotations. All letters appear in training (but only at even rotations). The validation set uses a designated validation letter (S in the main paper), evaluated on odd rotations. Test sets are formed from unseen test letters (W and Y in the main paper), also evaluated on odd rotations. Additional results with alternative validation/test letters are reported in the Table 5.

Subsampling for OT coupling. Each rendered silhouette contains many foreground pixels; to make mini-batch OT pairing tractable, we subsample a fixed number of points per cloud. We use $n = 100$ points per cloud because the discrete OT coupling has super-cubic complexity in n in our implementation, making larger clouds prohibitively expensive. This subsampling is applied consistently across all methods.

Key hyperparameters. Unless otherwise stated, we use: batch size 10, point subsampling $n = 100$, number of letters 4, number of rotations $R = 20$, number of colour replicas per condition $C = 100$, $(r_{\min}, r_{\max}) = (0.5, 0.6)$, and zero coordinate noise.

B.3 SP-FM implementation

B.4 SP-FM / PertFlow on Colored Letter Point Clouds

Data representation and conditions. Each sample is a point cloud of N points, where each point carries 2D geometry and RGB color:

$$\mathbf{x} = (x, y, r, g, b) \in \mathbb{R}^5, \quad \mathbf{X} \in \mathbb{R}^{N \times 5}.$$

We condition generation on the letter identity and rotation. The condition vector is

$$\mathbf{y} = [\text{one-hot}(\text{letter}), \rho] \in \mathbb{R}^C,$$

where $\rho \in [0, 1]$ is the normalized rotation angle (mapped to $[0, 2\pi]$ when decoding for visualization).

Dual-flow architecture (geometry vs. color). We use a dual-MLP conditional flow architecture: (i) a geometry flow v_{xy} acting on $(x, y) \in \mathbb{R}^2$ *per point*, and (ii) a color flow v_{rgb} acting on an RGB vector $(r, g, b) \in \mathbb{R}^3$ *per cloud*. Concretely, we decompose each cloud as

$$\mathbf{X}_{xy} \in \mathbb{R}^{N \times 2}, \quad \mathbf{c} \in \mathbb{R}^{1 \times 3},$$

where \mathbf{c} denotes the (shared) RGB color of the cloud (in our setup, all points in a cloud share the same color). Both velocity fields are implemented as MLPs that take time t and the concatenation of state and condition:

$$v_{xy}(t, \mathbf{x}_{xy}; \mathbf{y}) = \text{MLP}_{xy}(t, [\mathbf{x}_{xy}, \mathbf{y}]), \quad v_{rgb}(t, \mathbf{c}; \mathbf{y}) = \text{MLP}_{rgb}(t, [\mathbf{c}, \mathbf{y}]).$$

Conditional base distribution with random per-condition mode initialization. To sample the initial state \mathbf{X}_0 we use a condition-dependent mixture base. In the `use_kmeans=True` setting, mixture *centers* are initialized by **randomly sampling** K training point clouds for each condition \mathbf{y} (i.e., for each letter-rotation pair), rather than running K-means. These sampled clouds serve as fixed centers, while the mixture weights are predicted by a small network $h_p(\mathbf{y})$. At sampling time we draw a (soft) mixture over centers via Gumbel-Softmax (temperature τ) and add Gaussian perturbation with variance σ^2 to obtain $\mathbf{X}_{0,xy}$.

For color, we initialize a single RGB value per cloud by sampling uniformly from a predefined range $[a, b] \subset [0, 1]$ and broadcasting it to all points:

$$\mathbf{c}_0 \sim \mathcal{U}([a, b]^3), \quad \mathbf{X}_{0,rgb} = \mathbf{1}_N \mathbf{c}_0,$$

and finally concatenate geometry and color to obtain $\mathbf{X}_0 = [\mathbf{X}_{0,xy}, \mathbf{X}_{0,rgb}] \in \mathbb{R}^{N \times 5}$.

OT pairing. Before computing training losses, we align points between the sampled source cloud \mathbf{X}_0 and the target cloud \mathbf{X}_1 using point-wise optimal transport (OT) within each sample, which reduces sensitivity to arbitrary point ordering.

Flow matching objective. Given an OT-aligned pair $(\mathbf{X}_0, \mathbf{X}_1)$ under condition \mathbf{y} , we sample $t \sim \mathcal{U}[0, 1]$ and define

$$\mathbf{X}_t = (1 - t)\mathbf{X}_0 + t\mathbf{X}_1, \quad \mathbf{U} = \mathbf{X}_1 - \mathbf{X}_0.$$

We use the standard flow-matching regression form

$$\mathcal{L}_{\text{FM}} = \mathbb{E} \left[\|v(t, \mathbf{X}_t; \mathbf{y})\|_2^2 - 2\langle v(t, \mathbf{X}_t; \mathbf{y}), \mathbf{U} \rangle \right].$$

With the dual architecture, we compute this loss separately for geometry and color and sum them:

$$\mathcal{L}_{\text{FM}} = \mathcal{L}_{\text{FM}}^{\text{xy}} + \mathcal{L}_{\text{FM}}^{\text{rgb}},$$

where $\mathcal{L}_{\text{FM}}^{\text{xy}}$ is evaluated over all N points, and $\mathcal{L}_{\text{FM}}^{\text{rgb}}$ is evaluated on the single RGB vector per cloud.

Geodesic-length loss (default endpoint loss). In addition, we employ a shortest-path regularizer using the **default endpoint loss** (as in our configuration):

$$\mathcal{L}_{\text{geo}} = \mathbb{E} [\|\mathbf{X}_1 - \mathbf{X}_0\|_2^2].$$

In the dual setting, this decomposes as

$$\mathcal{L}_{\text{geo}} = \mathcal{L}_{\text{geo}}^{\text{xy}} + \mathcal{L}_{\text{geo}}^{\text{rgb}}, \quad \mathcal{L}_{\text{geo}}^{\text{xy}} = \mathbb{E} [\|\mathbf{X}_{1,xy} - \mathbf{X}_{0,xy}\|_2^2], \quad \mathcal{L}_{\text{geo}}^{\text{rgb}} = \mathbb{E} [\|\mathbf{c}_1 - \mathbf{c}_0\|_2^2].$$

Overall training objective. We optimize the combined objective

$$\mathcal{L} = \mathcal{L}_{\text{FM}} + \lambda \mathcal{L}_{\text{geo}},$$

with λ controlling the strength of the geodesic-length regularization.

B.5 GMM implementation

Table 5: Results on two synthetic experiments based on the letter S and letter H silhouettes. Each experiment assesses a model’s ability to generalize to rotations of the corresponding shape that are not observed during training.

Dataset	Model	Generated vs. Target			Source vs. Target		
		MMD ↓	W1 ↓	W2 ↓	MMD ↓	W1 ↓	W2 ↓
Letter H (Validation)	CFM	0.02021 ± 0.00115	0.7044 ± 0.0222	0.8626 ± 0.0229	0.09731 ± 0.00101	1.2101 ± 0.0056	1.3342 ± 0.0066
	SP-FM	0.01387 ± 0.00092	0.5939 ± 0.0190	0.7372 ± 0.0198	0.02773 ± 0.00042	0.7631 ± 0.0053	0.9048 ± 0.0047
Letter W (Test)	CFM	0.01778 ± 0.00101	0.6118 ± 0.0187	0.7219 ± 0.0203	0.06088 ± 0.00049	0.8972 ± 0.0062	1.0151 ± 0.0071
	SP-FM	0.01352 ± 0.00143	0.5429 ± 0.0196	0.6441 ± 0.0167	0.01872 ± 0.00062	0.6140 ± 0.0091	0.7173 ± 0.0099
Letter Y (Test)	CFM	0.02648 ± 0.00230	0.6669 ± 0.0295	0.7779 ± 0.0390	0.06020 ± 0.00128	1.0614 ± 0.0048	1.2407 ± 0.0055
	SP-FM	0.01735 ± 0.00167	0.5406 ± 0.0259	0.6358 ± 0.0295	0.04134 ± 0.00221	0.9525 ± 0.0399	1.1096 ± 0.0448